 doi: 10.1111/j.1365-246X.2009.04088.x

3-D dynamic rupture simulations by a finite volume method

M. Benjemaa,[1]* N. Glinsky-Olivier,[1] V. M. Cruz-Atienza[3,]† and J. Virieux[2]

[1] *INRIA-ENPC, CAIMAN project, Sophia-Antipolis, France. E-mail: mondher.benjemaa@gmail.com*
[2] *Laboratoire de Géophysique Interne et Tectonophysique, UJF, CNRS, Grenoble, France*
[3] *Department of Geological Sciences, San Diego State University, USA*

Accepted 2009 January 2. Received 2008 December 29; in original form 2008 January 22

SUMMARY

Dynamic rupture of a 3-D spontaneous crack of arbitrary shape is investigated using a finite volume (FV) approach. The full domain is decomposed in tetrahedra whereas the surface, on which the rupture takes place, is discretized with triangles that are faces of tetrahedra. First of all, the elastodynamic equations are described into a pseudo-conservative form for an easy application of the FV discretization. Explicit boundary conditions are given using criteria based on the conservation of discrete energy through the crack surface. Using a stress-threshold criterion, these conditions specify fluxes through those triangles that have suffered rupture. On these broken surfaces, stress follows a linear slip-weakening law, although other friction laws can be implemented. For The Problem Version 3 of the dynamic-rupture code verification exercise conducted by the SCEC/USGS, numerical solutions on a planar fault exhibit a very high convergence rate and are in good agreement with the reference one provided by a finite difference (FD) technique. For a non-planar fault of parabolic shape, numerical solutions agree satisfactorily well with those obtained with a semi-analytical boundary integral method in terms of shear stress amplitudes, stopping phases arrival times and stress overshoots. Differences between solutions are attributed to the low-order interpolation of the FV approach, whose results are particularly sensitive to the mesh regularity (structured/unstructured). We expect this method, which is well adapted for multiprocessor parallel computing, to be competitive with others for solving large scale dynamic ruptures scenarios of seismic sources in the near future.

Key words: Numerical approximations and analysis; Body waves; Wave propagation; Rheology and friction of fault zones; Dynamics and mechanics of faulting.

1 INTRODUCTION

Understanding the physics of the rupture process requires accurate methods able to take into account the geometry of the ruptured surface as well as realistic friction laws on this surface. Recent formulations have been proposed for modelling the dynamic shear crack rupture when considering the complexity of earthquake mechanisms embedded in heterogeneous crustal structure (Cruz-Atienza & Virieux 2004; Huang & Costanzo 2004). Almost all results have been obtained with boundary integral methods (Das & Aki 1977; Andrews 1985; Bécache & Duong 1994; Tada & Yamashita 1997; Tada & Madariaga 2001), which are highly adaptive and accurate to solve problems with complex fault geometries. Unfortunately, these methods used to be expensive since they required the computation of a spatio-temporal convolution proportional to the square of the grid elements number at each time step. Moreover, the analytic Green function involved in the convolution is only relevant for homogeneous medium. Finite element methods (Day 1977; Aagaard *et al.* 2001; Oglesby & Archuleta 2003), especially spectral formulations (Komatitsch & Vilotte 1998), are quite accurate in handling spontaneous propagation while considering complex crack structure (Festa & Vilotte 2006) but remain expensive in CPU memory or mesh construction. The finite difference methods (Andrews 1976, 1999; Madariaga 1976; Day 1982; Virieux & Madariaga 1982; Day *et al.* 2005; Dalguer & Day 2007) are fast and accurate enough but limited to rather simple fault geometries.

*Now at: École des mines de Paris, France.
†Now at: Departamento de Sismología Instituto de Geofísica, UNAM, Mexico.

Recently, Cruz-Atienza *et al.* (2007) have developped a new approach, called the finite difference fault element (FDFE) to overcome such limitation due to the cartesian grid discretization at the expense of a fine grid mesh and Ely *et al.* (2008, unpublished data) have introduced an efficient finite element technique based on finite difference operators for arbitrary shapes of faults. Benjemaa *et al.* (2007) have proposed, as well, an approach based on a finite volume (FV) formulation applied to 2-D shear rupture problems. We propose here the extension of this approach to the 3-D space for the spontaneous crack growth problem with specific 3-D implementations of boundary conditions.

The paper is organized as follows. In the first section, we introduce the elastodynamic system as well as the theoretical formulation of the boundary conditions on the fault surface. The second section is dedicated to the validation of the model. We study two different test cases: a planar fault that is compared with FD solutions obtained by Day *et al.* (2005) and a non-planar fault, for which our solution is compared with those computed by Cruz-Atienza *et al.* (2007) using a boundary integral equation (BIE) method (Aochi *et al.* 2000). The good agreement between results will confirm the robustness of our model.

2 ELASTODYNAMIC EQUATIONS

Let us first consider the FV formulation of a fracture problem in a linearly elastic infinite medium. Let us define a surface Γ, across which the particule displacement vector (and therefore the particle velocity vector) may have an unknown discontinuity. Appropriate stress conditions following prescribed friction law on this surface should be specified on this surface. More specifically, and throughout the paper, we may consider a linear slip weakening friction (SWF) law as a simple law to be implemented, although considering more complex ones is possible in our formulation.

2.1 Governing equations

Inside an infinite domain Ω but away from the fracture surface Γ, the medium is governed by the following velocity-stress linearized equations:

$$\rho \partial_t \vec{\boldsymbol{v}} = \operatorname{div} \underline{\sigma} \tag{1}$$

$$\partial_t \underline{\sigma} = \lambda \operatorname{div} \vec{\boldsymbol{v}}\, \mathbb{I}_3 + \mu \left[\vec{\nabla}\, \vec{\boldsymbol{v}} + \left(\vec{\nabla}\, \mathbf{v} \right)^t \right], \tag{2}$$

where $\mathbb{I}_3$ denotes the identity matrix, $\mathbf{v}$ the velocity vector and $\underline{\sigma}$ the symmetric stress tensor, both at each point of the medium. The spatially varying density is denoted by ρ and the Lamé coefficients by λ and μ. The subscript t denotes the time derivative whereas the superscript t means the transposition operation.

This system describes the elastic waves propagation in a heterogeneous medium (Madariaga 1976; Aki & Richards 1980; Virieux 1986). The initial conditions at each point $\mathbf{x}$ of the domain Ω are given by

$$\mathbf{v}(0,\ \mathbf{x}) = \mathbf{0}, \tag{3}$$

$$\underline{\sigma}(0,\ \mathbf{x}) = \underline{\sigma}_0, \tag{4}$$

where $\underline{\sigma}_0$ could be defined inside the medium from previous loading histories (Virieux & Madariaga 1982).

2.2 Crack boundary conditions

The crack surface Γ, which may have a complex geometry, is piecewise discretized and a normal vector $\mathbf{n}$ is defined at each face of the crack surface (see Fig. 10 for instance). We suppose a linearly elastic response of the entire medium except over the sliding surface Γ, where deformations and stresses are related through a friction law. In other words, the tangential stress to the crack surface Γ, also called the shear stress, is assumed to drop down to the dynamic frictional level, using a specific constitutive law we shall discuss later.

Let us first introduce some useful notations. Let $\mathbf{X}$ and $\mathbf{n}$ be two vectors. We define the normal and the tangential parts of $\mathbf{X}$ with respect to $\mathbf{n}$ [i.e. relative to the basis $(\mathbf{n}, \mathbf{n}^{\perp})$], respectively, by

$$\mathbf{X}_N = (\mathbf{n}^t\, \mathbf{X})\mathbf{n}, \tag{5}$$

$$\mathbf{X}_T = \mathbf{X} - \mathbf{X}_N = \mathbf{X} - (\mathbf{n}^t\, \mathbf{X})\mathbf{n}. \tag{6}$$

Because we allow the velocity to be discontinuous across the surface Γ, we define limiting values of the velocity vector as

$$\mathbf{v}^{\pm}(t,\ \mathbf{x}) = \lim_{\epsilon \to 0} \mathbf{v}\,(t,\ \mathbf{x} \pm \epsilon\ \mathbf{n}\,(\mathbf{x})). \tag{7}$$

The slip velocity vector $\mathbf{V}$ is defined as the tangential velocity discontinuity across the surface Γ,

$$\mathbf{V} := [\![\mathbf{v}_T]\!] = \mathbf{v}_T^+ - \mathbf{v}_T^-. \tag{8}$$

We then define the slip magnitude at time t as follows

$$U(t) = \int_0^t \| \mathbf{V}\,(s,\ \mathbf{x}) \|\ \mathrm{d}s. \tag{9}$$

Using these definitions, we now formulate the jump conditions on the crack surface as

$$\tau_c - \| \mathbf{T}_T \| \geq 0, \tag{10}$$

$$\tau_c \, \mathbf{V} - \mathbf{T}_T \, \| \mathbf{V} \| = \mathbf{0}, \tag{11}$$

where the vector $\mathbf{T}_T$ is the tangential projection of the traction vector $\mathbf{T} := \underline{\sigma}\mathbf{n}$. The quantity τ_c denotes the frictional strength, which evolves as a function of the fault normal stress $\sigma_N = \mathbf{n}^t \underline{\sigma} \mathbf{n}$ and the frictional coefficient $\boldsymbol{\mu}$:

$$\tau_c = -\sigma_N \, \boldsymbol{\mu} \, . \tag{12}$$

The friction coefficient $\boldsymbol{\mu}$ is here assumed to follow a linear slip weakening law given by

$$\boldsymbol{\mu}(U) = \mu_{\mathrm{d}} + (\mu_{\mathrm{s}} - \mu_{\mathrm{d}}) \left(1 - \frac{U}{\delta_0}\right) \mathrm{H}\left(1 - \frac{U}{\delta_0}\right). \tag{13}$$

In this equation, μ_{s} and μ_{d} are, respectively, the static and the dynamic friction coefficients, δ_0 is the critical slip weakening distance (Ida 1972; Palmer & Rice 1973) and H is the Heaviside function. Further explanations about the jump conditions (10) and (11) can be found in Andrews (1999) and Day *et al.* (2005).

3 FINITE VOLUME METHOD

Following the strategy used in Benjemaa *et al.* (2007) for the bidimensional case, we transform the system (1) and (2) into a pseudo-conservative formulation, to which we apply FV discretisation. Due to the symmetry of the stress tensor, one can easily split it into the sum of a trace tensor $\underline{\boldsymbol{s}}$ and a deviatoric tensor $\underline{\boldsymbol{d}}$, where

$$\underline{\boldsymbol{s}} = \frac{\sigma_{xx} + \sigma_{yy} + \sigma_{zz}}{3} \, \mathbb{I}_3 \tag{14}$$

and

$$\underline{\boldsymbol{d}} = \begin{pmatrix} \frac{1}{3}(2\,\sigma_{xx} - \sigma_{yy} - \sigma_{zz}) & \sigma_{xy} & \sigma_{xz} \\ \sigma_{xy} & \frac{1}{3}(-\sigma_{xx} + 2\,\sigma_{yy} - \sigma_{zz}) & \sigma_{yz} \\ \sigma_{xz} & \sigma_{yz} & \frac{1}{3}(-\sigma_{xx} - \sigma_{yy} + 2\,\sigma_{zz}) \end{pmatrix}. \tag{15}$$

We then define the stress vector $\boldsymbol{\sigma}$ as follows

$$\sigma = (\omega, \, \omega', \, \omega'', \, \sigma_{xy}, \, \sigma_{xz}, \, \sigma_{yz})^t \, , \tag{16}$$

where the quantities ω, ω' and ω'' derive directly from the trace and the deviatoric tensor:

$$\omega = \frac{1}{3}(\sigma_{xx} + \sigma_{yy} + \sigma_{zz}) \tag{17}$$

$$\omega' = \frac{1}{3}(2\,\sigma_{xx} - \sigma_{yy} - \sigma_{zz}) \tag{18}$$

$$\omega'' = \frac{1}{3}(-\sigma_{xx} + 2\,\sigma_{yy} - \sigma_{zz}). \tag{19}$$

This transformation enables us to group all medium properties on one hand of eq. (2), and the system (1) and (2) can be now written in a pseudo-conservative form:

$$\rho \, \partial_t \mathbf{v} = \sum_{\alpha \in \{x,\, y,\, z\}} (\partial_\alpha \mathbb{M}_\alpha) \, \sigma, \tag{20}$$

$$\Lambda \, \partial_t \sigma = \sum_{\alpha \in \{x,\, y,\, z\}} (\partial_\alpha \mathbb{N}_\alpha) \, \mathbf{v}, \tag{21}$$

where Λ is a diagonal matrix containing the material description,

$$\Lambda = \mathrm{diag}\left(\frac{3}{3\,\lambda + 2\,\mu}, \, \frac{3}{2\,\mu}, \, \frac{3}{2\,\mu}, \, \frac{1}{\mu}, \, \frac{1}{\mu}, \, \frac{1}{\mu}\right), \tag{22}$$

and the matrices $\mathbb{M}_\alpha$ and $\mathbb{N}_\alpha$ with $\alpha \in \{x, y, z\}$ are given by

$$\mathbb{M}_x = \begin{pmatrix} 1 & 1 & 0 & 0 & 0 & 0 \\ 0 & 0 & 0 & 1 & 0 & 0 \\ 0 & 0 & 0 & 0 & 1 & 0 \end{pmatrix}, \tag{23}$$

$$\mathbb{M}_y = \begin{pmatrix} 0 & 0 & 0 & 1 & 0 & 0 \\ 1 & 0 & 1 & 0 & 0 & 0 \\ 0 & 0 & 0 & 0 & 0 & 1 \end{pmatrix}, \tag{24}$$

$$\mathbb{M}_z = \begin{pmatrix} 0 & 0 & 0 & 0 & 1 & 0 \\ 0 & 0 & 0 & 0 & 0 & 1 \\ 1 & -1 & -1 & 0 & 0 & 0 \end{pmatrix}, \tag{25}$$

$$\mathbb{N}_x = \begin{pmatrix} 1 & 0 & 0 \\ 2 & 0 & 0 \\ -1 & 0 & 0 \\ 0 & 1 & 0 \\ 0 & 0 & 1 \\ 0 & 0 & 0 \end{pmatrix}, \tag{26}$$

$$\mathbb{N}_y = \begin{pmatrix} 0 & 1 & 0 \\ 0 & -1 & 0 \\ 0 & 2 & 0 \\ 1 & 0 & 0 \\ 0 & 0 & 0 \\ 0 & 0 & 1 \end{pmatrix}, \tag{27}$$

and

$$\mathbb{N}_z = \begin{pmatrix} 0 & 0 & 1 \\ 0 & 0 & -1 \\ 0 & 0 & -1 \\ 0 & 0 & 0 \\ 1 & 0 & 0 \\ 0 & 1 & 0 \end{pmatrix}. \tag{28}$$

Let us underline that the right-hand side (RHS) of the eqs (20) and (21) does not depend on the medium properties description. This new set of variables allows a non-ambiguous space integration, even when the medium contains heterogeneities.

3.1 Domain discretisation and finite volume scheme

The elastic medium Ω is discretized into tetrahedral finite volumes, called cells, in such a way that the crack surface Γ coincides with faces of specific cells at any time. This is quite realistic as one may consider that the crack usually ruptures on a pre-specified, mechanically weak zone surface of the earth crust, which may take millions of years to be localized. Therefore, the initial meshing of the entire medium could be such that any evolution of the crack surface will match numerical faces of cells.

The finite volume method supposes that the unknown variables are constant in each cell. Integrating the conservative form (20) and (21) over a cell $\mathcal{T}_i$ and applying the divergence theorem, we obtain

$$\int_{\mathcal{T}_i} \rho\, \partial_t \mathbf{v}\, \mathrm{d}V = \int_{\partial\mathcal{T}_i} \left(\sum_{\alpha\in\{x,y,z\}} (\mathbb{M}_\alpha\, n_\alpha)\, \sigma \right) \mathrm{d}S, \tag{29}$$

$$\int_{\mathcal{T}_i} \Lambda\, \partial_t \sigma\, \mathrm{d}V = \int_{\partial\mathcal{T}_i} \left(\sum_{\alpha\in\{x,y,z\}} (\mathbb{N}_\alpha\, n_\alpha)\, \mathbf{v} \right) \mathrm{d}S, \tag{30}$$

where $\partial\mathcal{T}_i$ represents the boundary of the cell $\mathcal{T}_i$ and $\mathbf{n}$ is the unitary outwards normal vector to $\mathcal{T}_i$. Assuming both the solution $\mathbf{v}$ and $\boldsymbol{\sigma}$ and the medium characteristic ρ, λ and μ constant in each cell $\mathcal{T}_i$, system (29) and (30) can be approximated by

$$V_{\mathcal{T}_i}\, \rho_{\mathcal{T}_i}\, (\partial_t \mathbf{v})_{\mathcal{T}_i} = \sum_{\mathcal{T}_k\in V(\mathcal{T}_i)} \sum_{\alpha\in\{x,y,z\}} \int_{\mathcal{T}_{ik}} \left((\mathbb{M}_\alpha\, n_{\alpha_{ik}})\, \sigma_{|_{\mathcal{T}_{ik}}} \right) \mathrm{d}S, \tag{31}$$

$$V_{\mathcal{T}_i}\, \Lambda_{\mathcal{T}_i}\, (\partial_t \sigma)_{\mathcal{T}_i} = \sum_{\mathcal{T}_k\in V(\mathcal{T}_i)} \sum_{\alpha\in\{x,y,z\}} \int_{\mathcal{T}_{ik}} \left((\mathbb{N}_\alpha\, n_{\alpha_{ik}})\, \mathbf{v}_{|_{\mathcal{T}_{ik}}} \right) \mathrm{d}S, \tag{32}$$

where the volume $V_{\mathcal{T}_i}$ is the volume of the cell $\mathcal{T}_i$, $V(\mathcal{T}_i)$ is the set of neighbouring cells of $\mathcal{T}_i$ (i.e. cells that share a common face with $\mathcal{T}_i$), $\mathcal{T}_{ik} = \mathcal{T}_i \cap \mathcal{T}_k$ is the interface between $\mathcal{T}_i$ and $\mathcal{T}_k$, $\mathbf{n}_{ik}$ is the unitary normal vector to $\mathcal{T}_{ik}$, pointed from $\mathcal{T}_i$ to $\mathcal{T}_k$, and $\sigma_{|_{\mathcal{T}_{ik}}}$ and $\mathbf{v}_{|_{\mathcal{T}_{ik}}}$ denote, respectively, the restriction of $\boldsymbol{\sigma}$ and $\mathbf{v}$ on the surface $\mathcal{T}_{ik}$. For convenience, we shall use from now, the index i to refer to the cell $\mathcal{T}_i$.

The approximation of the integral quantities in (31) and (32) is performed with a centred scheme. In other words, we consider the following approximation:

$$\sigma_{|\mathcal{T}_{ik}} \simeq \frac{\sigma_i + \sigma_k}{2}, \tag{33}$$

$$\mathbf{v}_{|\mathcal{T}_{ik}} \simeq \frac{\mathbf{v}_i + \mathbf{v}_k}{2}. \tag{34}$$

Using these approximations and the fact that we have assumed that σ_i and $\mathbf{v}_i$ are constant in $\mathcal{T}_i$, we can remove the quantities $\sigma_{|\mathcal{T}_{ik}}$ and $\mathbf{v}_{|\mathcal{T}_{ik}}$ from the integrals. On the other hand, if we denote the area of $\mathcal{T}_{ik}$ by S_{ik}, one can easily check the following identity

$$\int_{\mathcal{T}_{ik}} \mathbf{n}_{ik}\, dS = S_{ik}\, \mathbf{n}_{ik}. \tag{35}$$

Hence, we can rewrite the system (31) and (32) as

$$V_i\, \rho_i\, (\partial_t \mathbf{v})_i = \sum_{k \in V(i)} \sum_{\alpha \in \{x,\, y,\, z\}} S_{ik} (\mathbb{M}_\alpha\, n_{\alpha_{ik}}) \frac{\sigma_i + \sigma_k}{2}, \tag{36}$$

$$V_i\, \Lambda_i\, (\partial_t \sigma)_i = \sum_{k \in V(i)} \sum_{\alpha \in \{x,\, y,\, z\}} S_{ik} (\mathbb{N}_\alpha\, n_{\alpha_{ik}}) \frac{\mathbf{v}_i + \mathbf{v}_k}{2}, \tag{37}$$

or similarly,

$$V_i\, \rho_i\, (\partial_t \mathbf{v})_i = \sum_{k \in V(i)} S_{ik} \mathbb{P}_{ik}\, \frac{\sigma_i + \sigma_k}{2}, \tag{38}$$

$$V_i\, \Lambda_i\, (\partial_t \sigma)_i = \sum_{k \in V(i)} S_{ik}\, \mathbb{Q}_{ik}\, \frac{\mathbf{v}_i + \mathbf{v}_k}{2}\,, \tag{39}$$

where

$$\begin{aligned} \mathbb{P}_{ik} &= \sum_{\alpha \in \{x,\, y,\, z\}} \mathbb{M}_\alpha\, n_{\alpha_{ik}} \\ &= \begin{pmatrix} n_{x_{ik}} & n_{x_{ik}} & 0 & n_{y_{ik}} & n_{z_{ik}} & 0 \\ n_{y_{ik}} & 0 & n_{y_{ik}} & n_{x_{ik}} & 0 & n_{z_{ik}} \\ n_{z_{ik}} & -n_{z_{ik}} & -n_{z_{ik}} & 0 & n_{x_{ik}} & n_{y_{ik}} \end{pmatrix}, \end{aligned} \tag{40}$$

and

$$\begin{aligned} \mathbb{Q}_{ik} &= \sum_{\alpha \in \{x,\, y,\, z\}} \mathbb{N}_\alpha\, n_{\alpha_{ik}} \\ &= \begin{pmatrix} n_{x_{ik}} & n_{y_{ik}} & n_{z_{ik}} \\ 2\, n_{x_{ik}} & -n_{y_{ik}} & -n_{z_{ik}} \\ -n_{x_{ik}} & 2\, n_{y_{ik}} & -n_{z_{ik}} \\ n_{y_{ik}} & n_{x_{ik}} & 0 \\ n_{z_{ik}} & 0 & n_{x_{ik}} \\ 0 & n_{z_{ik}} & n_{y_{ik}} \end{pmatrix}. \end{aligned} \tag{41}$$

For temporal integration, we use a leap-frog scheme, where velocity is discretized at half-integer time steps and stress at integer time steps:

$$(\partial_t \mathbf{v})_i \simeq \frac{\mathbf{v}_i^{\,n+\frac{1}{2}} - \mathbf{v}_i^{\,n-\frac{1}{2}}}{\Delta t}, \tag{42}$$

$$(\partial_t \sigma)_i \simeq \frac{\sigma_i^{\,n+1} - \sigma_i^{\,n}}{\Delta t}\,. \tag{43}$$

The space–time discretized system can therefore be written as a rather simple numerical system

$$\rho_i\, \mathbf{v}_i^{\,n+\frac{1}{2}} = \rho_i\, \mathbf{v}_i^{\,n-\frac{1}{2}} + \frac{\Delta t}{V_i} \sum_{k \in V(i)} S_{ik}\, \mathbb{P}_{ik}\, \frac{\sigma_i^{\,n} + \sigma_k^{\,n}}{2}, \tag{44}$$

$$\Lambda_i\, \sigma_i^{\,n+1} = \Lambda_i\, \sigma_i^{\,n} + \frac{\Delta t}{V_i} \sum_{k \in V(i)} S_{ik}\, \mathbb{Q}_{ik}\, \frac{\mathbf{v}_i^{\,n+\frac{1}{2}} + \mathbf{v}_k^{\,n+\frac{1}{2}}}{2}, \tag{45}$$

which turns out to have a lower number of elementary numerical operations than standard second-order FD schemes.

4 ENERGY CONSIDERATION

Eqs (44) and (45) are available everywhere inside the medium Ω except over the fault surface Γ. Indeed, boundary conditions (10) and (11) must be verified through Γ. For this purpose, we propose to identify the appropriate quantities that should be taken over Γ, by studying the energy of the system (44) and (45). Once this energy is established, we define fictitious cells above and below the fault surface that enforce the energy variation to be zero when no tractions are specified on Γ. Then we use the conditions (10) and (11) to complete the flux expressions when considering a tangential traction on the fault surface.

Let first note that the system (44) and (45) is not symmetric, because

$$\mathbb{Q}_{ik} \neq \mathbb{P}^t_{ik}, \tag{46}$$

as induced by the variable transformation introduced in (17)–(19). We recall that these transformations were made to group all the medium characteristics on the left-hand side of the eq. (21). Because it is far easier to deal with symmetric systems when considering energy computation since the energy of a partial differential equations is equivalent to a Lyapunov function (i.e. symmetric positive definite quadratic form) for the ordinary differential equations, we can obtain a symmetric system for (44) and (45) by multiplying equation (45) by the symmetric positive definite matrix $\mathbb{S}$ given by

$$\mathbb{S} = \begin{pmatrix} 1 & 0 & 0 & 0 & 0 & 0 \\ 0 & \frac{2}{3} & \frac{1}{3} & 0 & 0 & 0 \\ 0 & \frac{1}{3} & \frac{2}{3} & 0 & 0 & 0 \\ 0 & 0 & 0 & 1 & 0 & 0 \\ 0 & 0 & 0 & 0 & 1 & 0 \\ 0 & 0 & 0 & 0 & 0 & 1 \end{pmatrix}. \tag{47}$$

One can check in this case that

$$\mathbb{S}\,\mathbb{Q}_{ik} = \mathbb{P}^t_{ik}, \tag{48}$$

which gives us an equivalent symmetric system to the system (44) and (45) as

$$\rho_i \mathbf{v}_i^{n+\frac{1}{2}} = \rho_i \mathbf{v}_i^{n-\frac{1}{2}} + \frac{\Delta t}{V_i} \sum_{k \in V(i)} S_{ik}\, \mathbb{P}_{ik}\, \frac{\sigma_i^n + \sigma_k^n}{2}, \tag{49}$$

$$\mathbf{\Lambda}_i \sigma_i^{n+1} = \mathbf{\Lambda}_i \sigma_i^n + \frac{\Delta t}{V_i} \sum_{k \in V(i)} S_{ik}\, \mathbb{P}^t_{ik}\, \frac{\mathbf{v}_i^{n+\frac{1}{2}} + \mathbf{v}_k^{n+\frac{1}{2}}}{2}, \tag{50}$$

where the new matrix of material properties $\mathbf{\Lambda}_i$ is now $\mathbb{S}\,\Lambda_i$. For this symmetric system (49) and (50), we now define the discrete energy as

$$E^n = \frac{1}{2} \sum_i V_i \left[\rho_i \left(\mathbf{v}_i^{n-\frac{1}{2}} \right)^t \mathbf{v}_i^{n+\frac{1}{2}} + \sigma_i^n\, \mathbf{\Lambda}_i\, \sigma_i^n \right]. \tag{51}$$

The discrete energy time variation is given by

$$\begin{aligned} \Delta E^n &:= E^{n+1} - E^n \\ &= \frac{\Delta t}{2} \sum_{i,k \in \Gamma} S_{ik} \left[\left(\mathbf{v}_i^{n+\frac{1}{2}} \right)^t \mathbb{P}_{ik}\, \sigma_k^{[n+\frac{1}{2}]} + \left(\sigma_i^{[n+\frac{1}{2}]} \right)^t \mathbb{P}^t_{ik}\, \mathbf{v}_k^{n+\frac{1}{2}} \right], \end{aligned} \tag{52}$$

where the stress estimation at half-integer time steps is obtained through the following averaged expression

$$\sigma_i^{[n+\frac{1}{2}]} = \frac{\sigma_i^n + \sigma_i^{n+1}}{2}, \tag{53}$$

as shown in the appendix B of Benjemaa *et al.* (2007). If we set

$$\mathcal{F}^n_{ik} = \mathbb{P}_{ik}\, \frac{\sigma_i^n + \sigma_k^n}{2} \tag{54}$$

and

$$\mathcal{G}^{n+\frac{1}{2}}_{ik} = \mathbb{P}^t_{ik}\, \frac{\mathbf{v}_i^{n+\frac{1}{2}} + \mathbf{v}_k^{n+\frac{1}{2}}}{2}, \tag{55}$$

one can check that the energy time variation is reduced to the following expression

$$\Delta E^n = \Delta t \sum_{i,k \in \Gamma} S_{ik} \left[\left(\mathbf{v}_i^{n+\frac{1}{2}} \right)^t \left(\mathcal{F}^{[n+\frac{1}{2}]}_{ik} - \mathbb{P}_{ik}\, \sigma_i^{[n+\frac{1}{2}]} \right) + \left(\sigma_i^{[n+\frac{1}{2}]} \right)^t \mathcal{G}^{n+\frac{1}{2}}_{ik} \right]. \tag{56}$$

Whether ΔE^n is equal to zero or not does not appear clearly in eq. (56). In fact, ΔE^n must be at least less or equal to zero to insure the stability of the elastodynamic system. Since the sum in the expression (56) is only concerned with cells with interfaces belonging to the fault surface Γ, flux expressions (54) and (55) have to be modified so that boundary conditions are verified on this surface. The eq.(54)

Table 1. Elastic properties of the medium.

v_s (m s^{-1})	v_p (m s^{-1})	ρ (kg m^{-3})
3464	6000	2670

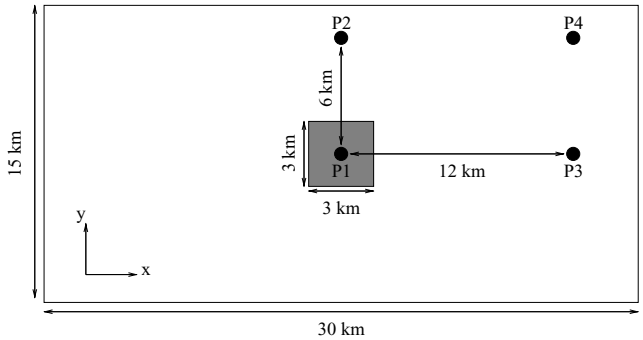

Figure 1. Fault model for testing dynamic rupture simulation for the SCEC problem. The grey square in the centre is the nucleation zone. The black circles are the receivers at which we compare time histories of the shear stress and the slip velocity.

(respectively 55) stipulates that the stress flux through an arbitrary interface $\mathcal{T}_{ik}$ is based on a centred scheme of the stress (respectively the velocity) values above and below this interface. This can no longer be true if the face $\mathcal{T}_{ik}$ belong to Γ, since the fault is a surface where discontinuities may occur. For this reason, we rewrite the eqs (54) and (55) in a more general form as follow:

$$\mathcal{F}_{ik}^{n} = \frac{1}{2}\,\mathbb{P}_{ik}\,\sigma_i^{\,n} + \frac{1}{2}\,(\mathbb{A}_{ik}\,\sigma_i^{\,n} + \mathbb{B}_{ik}\,\sigma_k^{\,n}), \tag{57}$$

$$\mathcal{G}_{ik}^{n+\frac{1}{2}} = \frac{1}{2}\,\mathbb{P}_{ik}^{t}\,\mathbf{v}_i^{\,n+\frac{1}{2}} + \frac{1}{2}\,(\mathbb{C}_{ik}\,\mathbf{v}_i^{\,n+\frac{1}{2}} + \mathbb{D}_{ik}\,\mathbf{v}_k^{\,n+\frac{1}{2}}), \tag{58}$$

where the matrices $\mathbb{A}_{ik}$, $\mathbb{B}_{ik}$, $\mathbb{C}_{ik}$ and $\mathbb{D}_{ik}$ are to be determined for specific boundary conditions. Please note that we have kept original contributions of fields in cell i, and we have adapted contributions from the adjacent cell k as a possible combination of quantities from cell i and cell k. If we substitute the fluxes $\mathcal{F}_{ik}^{n}$ and $\mathcal{G}_{ik}^{n+\frac{1}{2}}$ by their expressions (57) and (58) in the eq. (56), we obtain

$$\begin{aligned}\Delta E^n = \frac{\Delta t}{2} \sum_{\substack{i,k/\\ \mathcal{T}_{ik}\subset\Gamma}} S_{ik} \Bigg[&\left(\mathbf{v}_i^{\,n+\frac{1}{2}}\right)^t \left(\mathbb{A}_{ik} + \mathbb{C}_{ik}^t\right) \sigma_i^{\,[n+\frac{1}{2}]} + \left(\mathbf{v}_k^{\,n+\frac{1}{2}}\right)^t \left(-\mathbb{B}_{ik} + \mathbb{D}_{ik}^t\right) \sigma_i^{\,[n+\frac{1}{2}]} \\ &- \left(\mathbf{v}_k^{\,n+\frac{1}{2}}\right)^t \left(\mathbb{A}_{ik} + \mathbb{C}_{ik}^t\right) \sigma_k^{\,[n+\frac{1}{2}]} - \left(\mathbf{v}_i^{\,n+\frac{1}{2}}\right)^t \left(-\mathbb{B}_{ik} + \mathbb{D}_{ik}^t\right) \sigma_k^{\,[n+\frac{1}{2}]} \Bigg],\end{aligned} \tag{59}$$

where the minus sign comes from the fact that $\mathbf{n}_{ki} = -\mathbf{n}_{ik}$. The energy variation ΔE^n is then equal to zero if the following equalities hold:

$$\mathbb{A}_{ij} + \mathbb{C}_{ij}^t = 0, \tag{60}$$

$$\mathbb{B}_{ij} - \mathbb{D}_{ij}^t = 0. \tag{61}$$

Besides, one may check that

$$\mathbb{P}_{ik}\,\sigma_{[ik]} = \underline{\sigma}_{[ik]}\,\mathbf{n}_{ik}, \tag{62}$$

where the bracket subscript designs the mean value of the variables,

$$\gamma_{[ik]} = \frac{\gamma_i + \gamma_k}{2}, \qquad \gamma = \sigma, \underline{\sigma}. \tag{63}$$

The left-hand side of the eq. (62) is the stress flux through the interface $\mathcal{T}_{ik}$, whereas the RHS is the traction vector on this surface. Thus, the equality (62) simply shows that the flux $\mathcal{F}_{ik}$ is nothing but the traction vector on the surface $\mathcal{T}_{ik}$. The quantity $\mathcal{F}_{ik}^{n}$ can be written as the sum

Table 2. Frictional parameters on the fault.

Parameters	Nucleation	Outside nucleation
Initial shear stress σ_0 (MPa)	81.6	70
Initial normal stress $-\sigma_n$ (MPa)	120	120
Static friction coefficient $\boldsymbol{\mu_s}$	0.677	0.677
Dynamic friction coefficient $\mu_{\boldsymbol{d}}$	0.525	0.525
Static yielding stress $\sigma_s = -\boldsymbol{\mu_s}\,\sigma_n$ (MPa)	81.24	81.24
Dynamic yielding stress $\sigma_d = -\mu_{\boldsymbol{d}}\,\sigma_n$ (MPa)	63	63
Critical slip distance δ_0 (m)	0.4	0.4

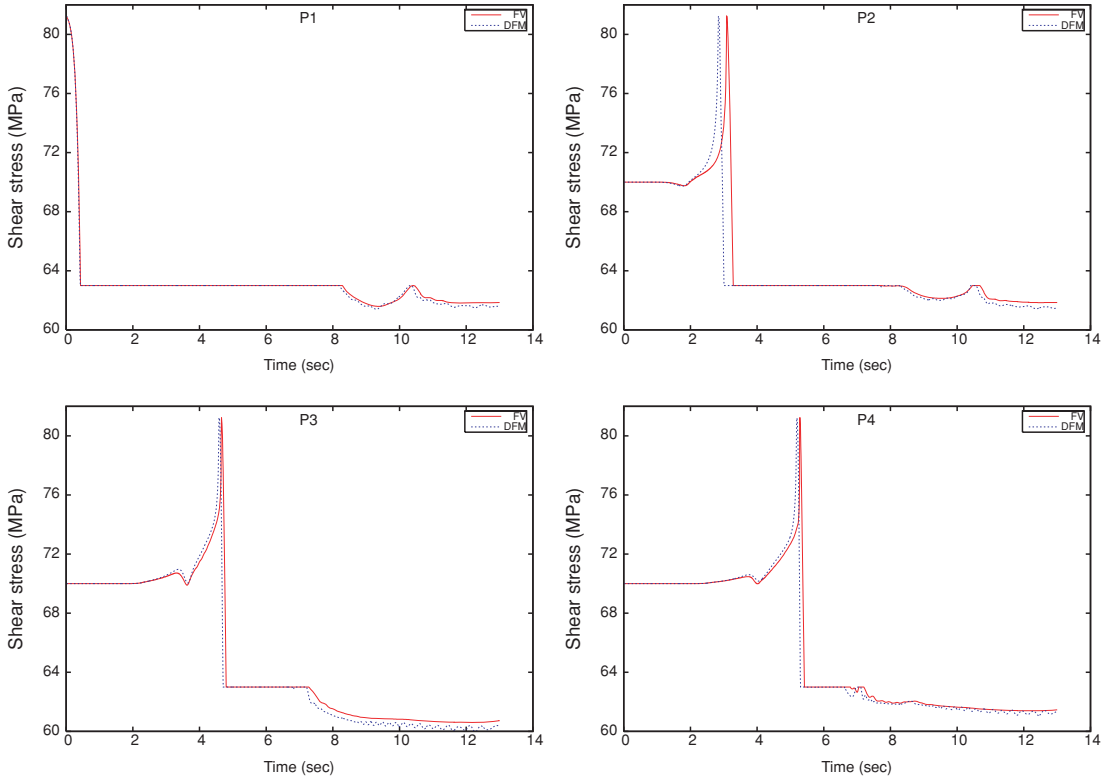

Figure 2. Comparison of the FV numerical solutions (red) and the DFM numerical solution (blue) of the shear stress in four points located on the fault surface. Global good agreement can be noted.

of its normal and tangential components,

$$\begin{aligned}\mathcal{F}_{ik}^{n} &= \mathcal{F}_{ik_N}^{n} + \mathcal{F}_{ik_T}^{n} \\ &= \left(\mathbf{n}_{ik}^{t}\,\mathbb{P}_{ik}\,\sigma_{[ik]}^{n}\right)\mathbf{n}_{ik} + \mathcal{F}_{ik_T}^{n}. \end{aligned} \tag{64}$$

When no tangential traction is applied on the surface $\mathcal{T}_{ik}$ (i.e. $\mathcal{F}_{ik_T} = 0$), the stress flux $\mathcal{F}_{ik}$ is reduced to its normal component, and the discrete energy must be constant. Equating expressions (57) and (64), one can deduce

$$\mathbb{A}_{ik} = \left(\mathbf{n}_{ik}\mathbf{n}_{ik}^{t} - \mathbb{I}_3\right)\mathbb{P}_{ik}, \tag{65}$$

$$\mathbb{B}_{ik} = \mathbf{n}_{ik}\mathbf{n}_{ik}^{t}\,\mathbb{P}_{ik}, \tag{66}$$

and, via eqs (60) and (61), we obtain

$$\mathbb{C}_{ik} = \mathbb{P}_{ik}^{t}\left(\mathbf{n}_{ik}\mathbf{n}_{ik}^{t} - \mathbb{I}_3\right), \tag{67}$$

$$\mathbb{D}_{ik} = \mathbb{P}_{ik}^{t}\,\mathbf{n}_{ik}\mathbf{n}_{ik}^{t}. \tag{68}$$

We have determined the geometrical expressions of the four matrices needed for boundary conditions, when no traction is applied on the fault surface. One may say that this surface is transparent to the numerical approximations of elastic waves, thank to the discrete energy conservation. Considering the spontaneous shear crack problem implies that the tangential traction is no more equal to zero, and therefore, we have to modify the eq. (64) of fluxes to take into account such a traction. We shall rewrite the eq. (64) as

$$\mathcal{F}_{ik}^{n} = \left(\mathbf{n}_{ik}^{t}\,\mathbb{P}_{ik}\,\sigma_{[ik]}^{n}\right)\mathbf{n}_{ik} + \mathbf{T}_{ik_T}^{n}, \tag{69}$$

where the vector $\mathbf{T}_{ik_T}^{n}$ denotes the tangential projection of the traction vector applied to the surface $\mathcal{T}_{ik}$ at time $n\Delta t$, which should verify the boundary conditions (10) and (11).

On another hand, eq. (44) can be written in general form as

$$\mathbf{v}_i^{n+\frac{1}{2}} = \mathbf{v}_i^{n-\frac{1}{2}} + \frac{\Delta t}{\rho_i\,V_i}\sum_{k\in\mathcal{V}(i)} S_{ik}\,\mathcal{F}_{ik}^{n}, \tag{70}$$

where $\mathcal{F}_{ik}^{n}$ is given by eq. (54) if the interface $\mathcal{T}_{ik}$ does not belong to the fault surface and is given by relation (69) if $\mathcal{T}_{ik}$ belongs to the fault surface. Recall that in the latter case, the tangential traction vector $\mathbf{T}_{ik_T}^{n}$ is still to be found out following the failure criterion (10) and (11).

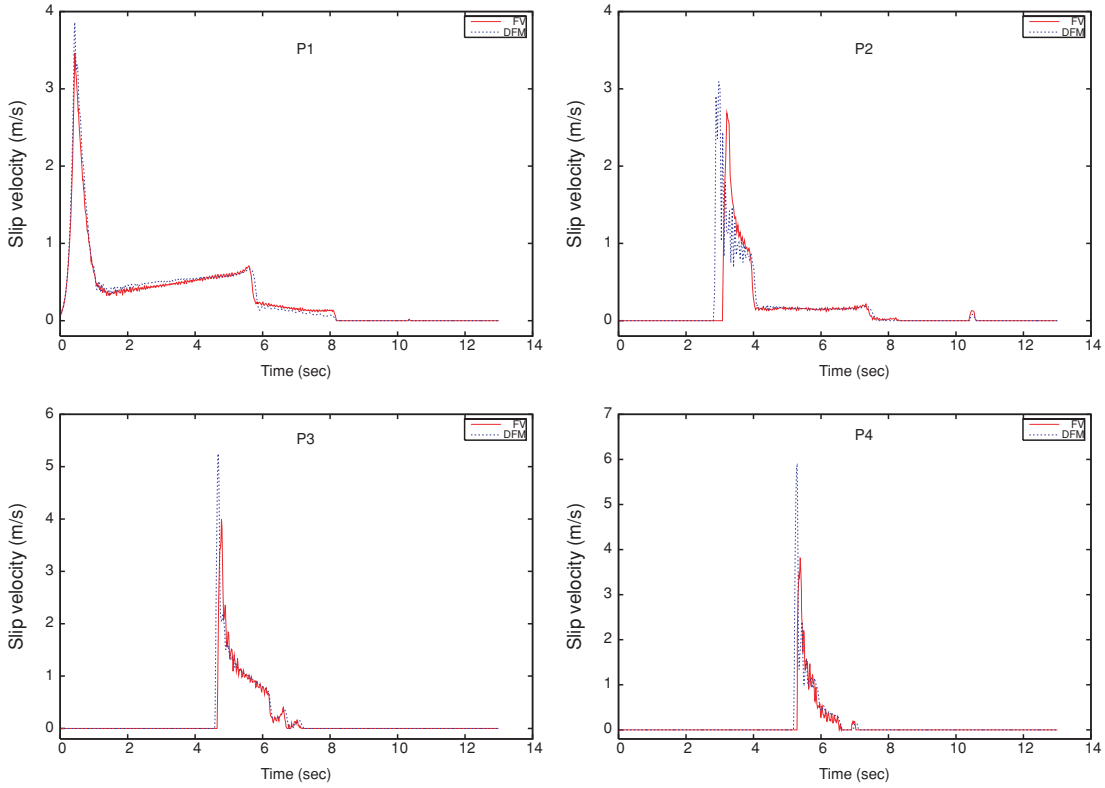

Figure 3. Comparison of the FV numerical solutions (red) and the DFM numerical solution (blue) of the slip velocity in four points located on the fault surface. The solutions are almost similar, eventhough the slip velocity peak seems to be underestimated for the FV approach. The solutions are presented with no special filtering treatment.

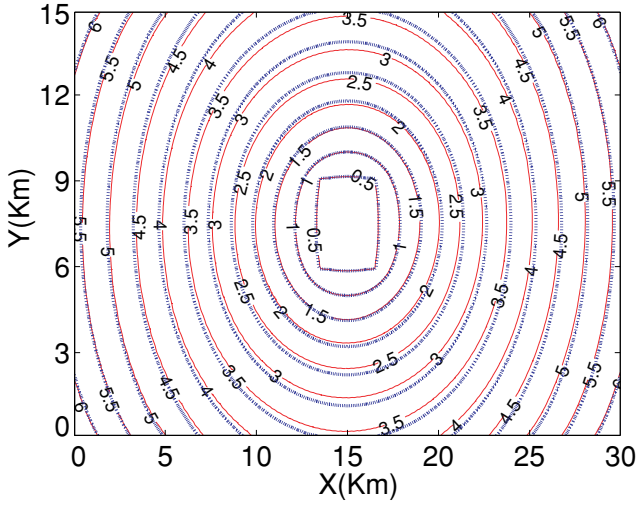

Figure 4. Rupture front contours at 0.5 s intervals computed along the fault surface for the FV (red) and the DFM (blue) methods. Good agreement of the time histories can be noted. The rupture seems to propagate at lower speed along the anti-plane direction for the FV method.

We now rewrite eq. (70) as follows:

$$\mathbf{v}_i^{n+\frac{1}{2}} = \mathbf{v}_i^{n-\frac{1}{2}} + \frac{\Delta t}{\rho_i\, V_i} \sum_{\substack{k\in V(i)\\ \mathcal{T}_i\cap\mathcal{T}_k\not\subset\Gamma}} S_{ik}\, \mathbb{P}_{ik}\, \frac{\sigma_i^n + \sigma_k^n}{2} + \frac{\Delta t}{\rho_i\, V_i} \sum_{\substack{k\in V(i)\\ \mathcal{T}_i\cap\mathcal{T}_k\subset\Gamma}} S_{ik}\, \mathcal{F}_{ik}^n\,, \tag{71}$$

where we have replaced the flux $\mathcal{F}_{ik}^n$ by its centred approximation (54), only for the interfaces that do not belong to the fault surface.

Let $\mathbf{R}_i^n$ be the quantity that involves no flux contribution from the fault surface:

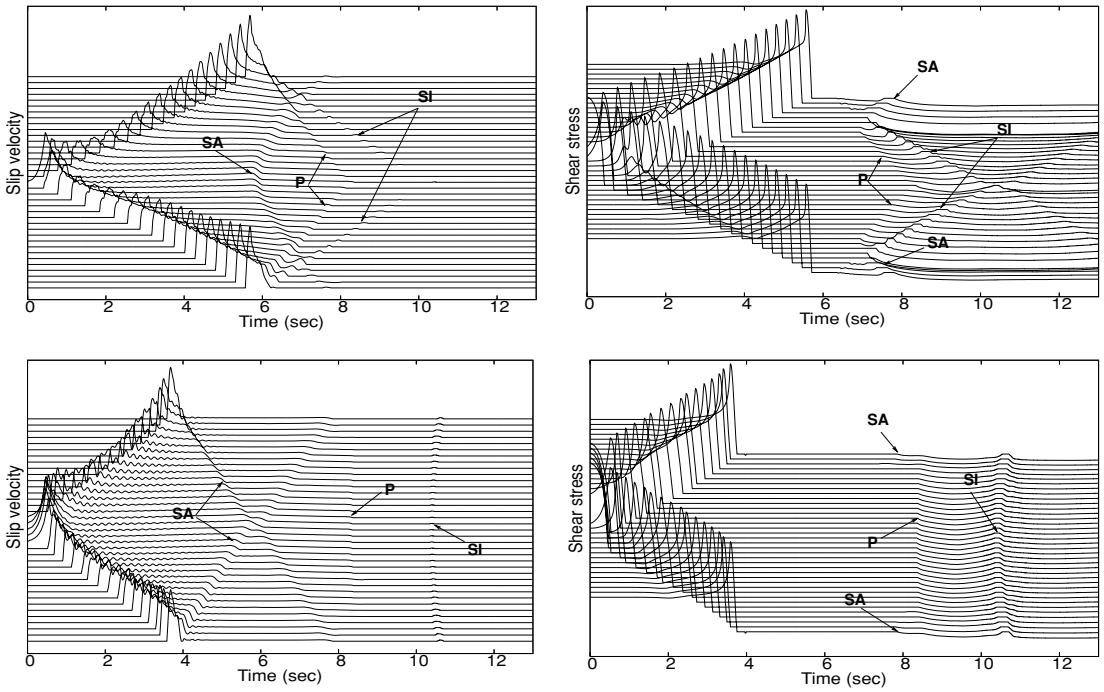

Figure 5. Time history of the slip velocity (left-hand panel) and the shear stress (right-hand panel) along the in-plane (top) and the antiplane (bottom) directions. *P* and *SI* are, respectively, the primary and secondary waves generated by the left- and right-hand edges of the fault. *SA* is the secondary wave generated by the top and the bottom edges of the fault.

$$\mathbf{R}_i^n = \frac{\Delta t}{\rho_i\, V_i} \sum_{\substack{k\in V(i)\\ \mathcal{T}_i\cap\mathcal{T}_k\not\subset\Gamma}} S_{ik}\, \mathbb{P}_{ik}\, \frac{\sigma_i^n + \sigma_k^n}{2}\,. \tag{72}$$

Eq. (71) can then be written as

$$\mathbf{v}_i^{n+\frac{1}{2}} = \mathbf{v}_i^{n-\frac{1}{2}} + \mathbf{R}_i^n + \frac{\Delta t\, S_{ik}}{\rho_i\, V_i}\, \mathcal{F}_{ik}^n\,, \tag{73}$$

where $\mathcal{T}_i$ and $\mathcal{T}_k$ design two opposite cells sharing an interface $\mathcal{T}_{ik} \subset \Gamma$.

Now, assuming the inequality (10) is strict, that is,

$$\tau_c - \| \mathbf{T}_{ik_T} \| > 0\,, \tag{74}$$

and taking the modulus of eq. (11), one can deduce that

$$\mathbf{V}_{ik} = \mathbf{0}\,. \tag{75}$$

Or, using the eq. (73), the slip velocity vector $\mathbf{V}_{ik}$ is given by

$$\begin{aligned}\mathbf{V}_{ik}^{n+\frac{1}{2}} &:= \mathbf{v}_{i_T}^{n+\frac{1}{2}} - \mathbf{v}_{k_T}^{n+\frac{1}{2}}\\ &= \mathbf{V}_{ik}^{n-\frac{1}{2}} + \mathbf{R}_{i_T}^n - \mathbf{R}_{k_T}^n + \Delta t\, S_{ik} \left(\frac{1}{\rho_i\, V_i} + \frac{1}{\rho_k\, V_k}\right) \mathcal{F}_{ik_T}^n\\ &= \mathbf{V}_{ik}^{n-\frac{1}{2}} + \mathbf{R}_{i_T}^n - \mathbf{R}_{k_T}^n + \Delta t\, S_{ik} \left(\frac{1}{\rho_i\, V_i} + \frac{1}{\rho_k\, V_k}\right) \mathbf{T}_{ik_T}^n,\end{aligned} \tag{76}$$

which leads us, when it is equal to zero, to the following vector

$$\tilde{\mathbf{T}}_{ik_T}^n = \frac{\left(-\mathbf{V}_{ik}^{n-\frac{1}{2}} - \mathbf{R}_{i_T}^n + \mathbf{R}_{k_T}^n\right) \rho_i\, \rho_k\, V_i\, V_k}{\Delta t\, S_{ik}\, (\rho_i\, V_i + \rho_k\, V_k)}. \tag{77}$$

When introduced into the expression (76), this vector will enforce the continuity of the tangential velocity as it sets the slip velocity to zero. We are now able to define the traction vector as

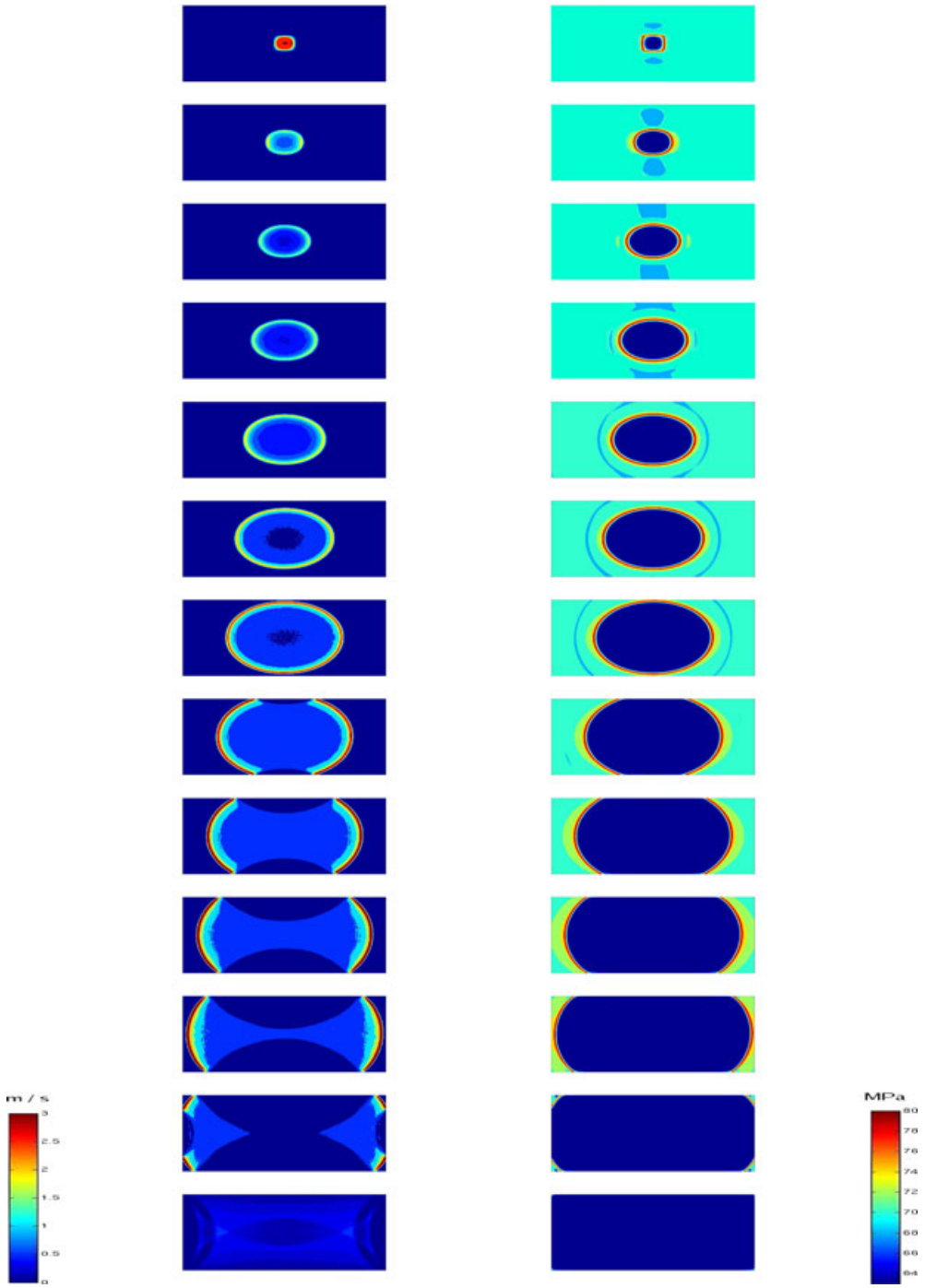

Figure 6. Snapshots of the slip velocity (left-hand panel) and the shear stress (right-hand panel) at 0.5 s time intervals along the fault.

$$\mathbf{T}^n_{ik_T} = \begin{cases} \tilde{\mathbf{T}}^n_{ik_T}, & \text{if } \| \tilde{\mathbf{T}}^n_{ik_T} \| < \tau_c \\ \dfrac{\tilde{\mathbf{T}}^n_{ik_T}}{\| \tilde{\mathbf{T}}^n_{ik_T} \|} \tau_c, & \text{if } \| \tilde{\mathbf{T}}^n_{ik_T} \| \geq \tau_c \,. \end{cases} \tag{78}$$

Finally, using eqs (57), (58), (65)–(69), we conclude that the fluxes through an interface $\mathcal{T}_{ik} \subset \Gamma$ are given by

$$\mathcal{F}^n_{ik} = \mathbf{n}_{ik} \mathbf{n}^t_{ik} \mathbb{P}_{ik} \frac{\sigma_i{}^n + \sigma_k{}^n}{2} + \mathbf{T}^n_{ik_T}, \tag{79}$$

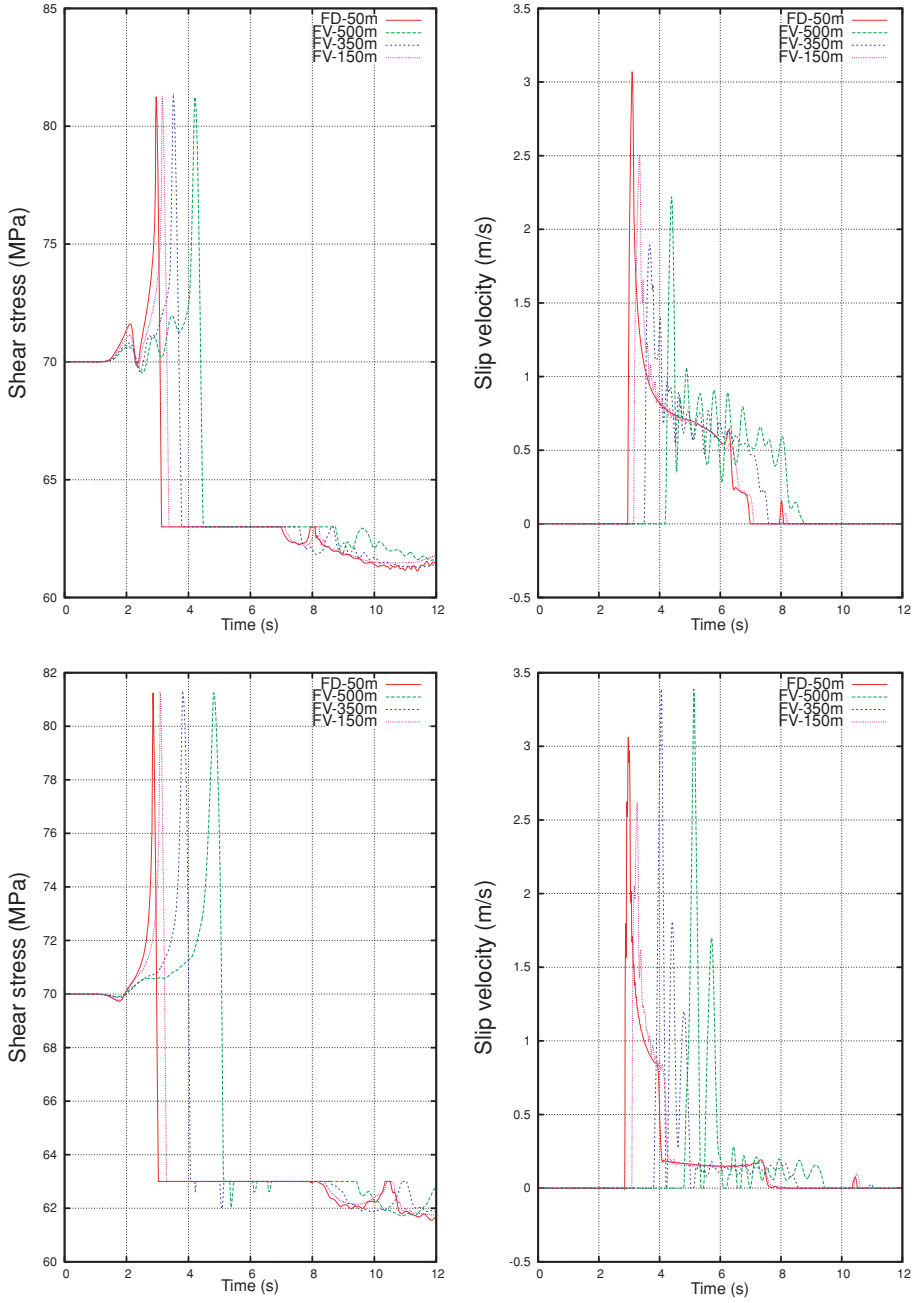

Figure 7. Comparison of the shear stress (left-hand panel) and the slip velocity (right-hand panel) for different mesh grids. The receivers are located at 7.5 km from the centre along the strike direction (top panels) and at 6 km from the centre along the dip direction (bottom panels), respectively. A numerical FD solution for this problem is taken as the reference solution (solid line). Obviously, the FV solutions converge to the reference solution as the grid mesh decreases.

$$\mathcal{G}_{ik}^{n+\frac{1}{2}} = \mathbb{P}_{ik}^{t}\left(\mathbf{v}_i^{n+\frac{1}{2}} - \mathbf{n}_{ik}\mathbf{n}_{ik}^{t}\frac{\mathbf{v}_i^{n+\frac{1}{2}} - \mathbf{v}_k^{n+\frac{1}{2}}}{2}\right), \tag{80}$$

where $\mathbf{T}_{ik_T}^{n}$ is given by the expression (78), for a face belonging to the Γ surface, allowing either continuous numerical velocity and stress fields or non-zero shear slip and discontinuous shear stress. Similar expressions could be constructed for different complex boundary conditions, as for the fracture mode I, for instance.

5 MODEL VALIDATION

To validate our method, we propose two comparisons between our numerical solutions and those obtained by other approaches: the dynamic fault model (DFM) developped by Day *et al.* (2005) and the boundary integral equation (BIE) method developped by Aochi *et al.* (2000). Since

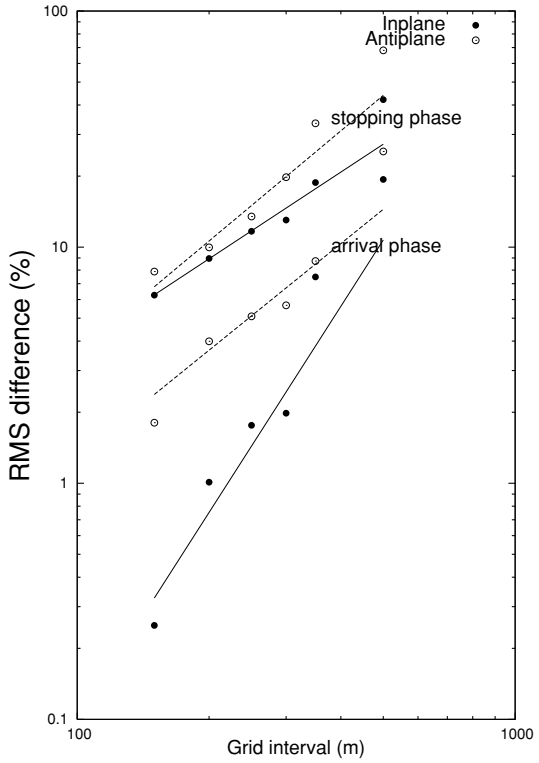

Figure 8. Difference in arrival time (bottom) and stopping phase (top) in two receivers for several mesh grids. The rms is computed relative to the FD time solutions obtained with a 50 m grid interval.

these methods are highly independent of each other and, particularly, of our finite volume method, we consider this comparison of numerical solutions as a relevant validation of our proposed method, since no analytical solutions are available for the spontaneous slip-weakening rupture problem.

5.1 Test problem 1

We consider a planar fault embedded in a linearly elastic homogeneous full-space. The formulation and parameters of this test case correspond to The Problem Version 3 (TPV3) of the Southern California Earthquake Centre (SCEC) code comparison exercise (Harris *et al.* 2009). The elastic propreties of the medium are listed in Table 1.

The fault geometry of this problem is detailed in Fig. 1. We consider the fault plane to be the xy plane and the rupture is allowed within a fault area of 30 km in the x direction and 15 km in the y direction. The shear pre-stress is aligned with the x axis. The stress initial conditions and the frictional parameters on the fault are given in Table 2.

For the initation of the rupture, we impose a 3×3 km square nucleation zone centred on the fault. The rupture initiates because we have set the initial shear stress slightly higher than the initial static yield stress in the nucleation zone. We assume an infinite static frictional stress outside the 30×15 km zone, which prohibits the propagation of the rupture beyond this surface.

We used for this simulation a structured mesh with space length equal to 0.15 km, leading to 160 millons of tetrahedra, and a time step $\Delta t = 6.5 \times 10^{-3}$ s, whereas the DFM method used a grid size $\Delta x = 0.1$ km and a time step $\Delta t = 8 \times 10^{-3}$ s, although direct comparisons of these quantities are meaningless. The calculation has been performed on 100 processors using message passing interface (MPI). The CPU time of the simulation is around 5×10^3 s.

We plot seismograms computed at four points located on the fault plane, as shown in Fig. 1. Figs 2 and 3 compare, respectively, the shear stress and the slip velocity numerical solutions of our approach and the DFM approach. One can see a good agreement between numerical solutions, even though the slip velocity seems to be underestimated by the finite volume method. We also note differences in the rupture time, especially in the antiplane direction. Let us remark that the triangular discretization of the fault surface could make the observational points slightly distant from their expected positions (i.e. comparatively to the cartesian grid used by the FD method). This difference could be reduced if the mesh is refined enough along the fault surface.

Fig. 4 shows a comparison of rupture time contours for both approaches. One can see that the rupture propagates at almost the same speed. The level of agreement appears to be good if one takes into consideration the relative error due to the irregular distribution of the points on the fault surface. Small differences are noted at long time, especially in the antiplane direction.

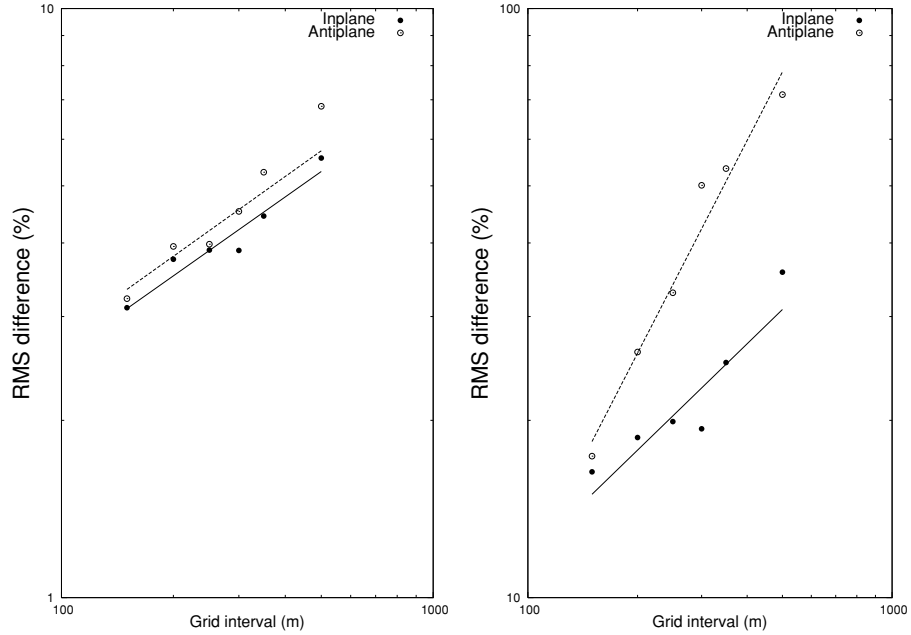

Figure 9. RMS in time for the shear stress (left-hand panel) and the shifted phase slip velocity (right-hand panel) for different mesh grids comparative to the FD numerical solution. The FV solutions converge to the reference solution as the grid mesh decreases. Apparent difference in the slope, especially for the slip velocity, is due to high numerical oscillations in the antiplane propagation direction (see Fig. 7 for instance).

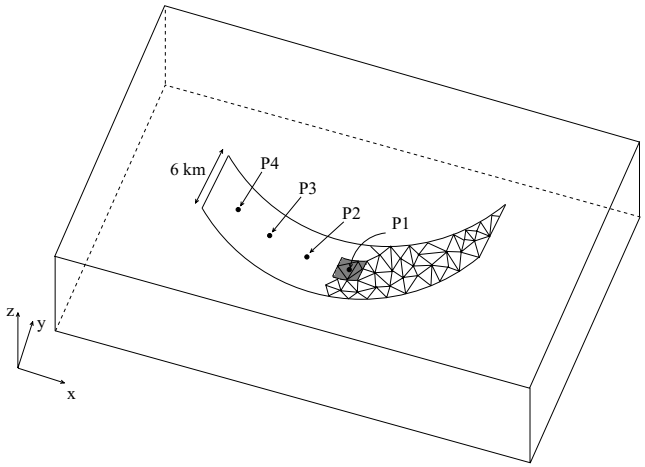

Figure 10. 3-D view of a non planar crack surface. The grey 'square' region of 2 km sides length centred along the strike and dip directions represents the nucleation zone. The four observational points aligned with the dip direction are separated by 4 km measured along the fault surface from each other. The fault surface is discretized by triangles as partly shown on the figure.

Fig. 5 describes the slip velocity and the shear stress time history profiles along the *x*- (in-plane direction) and the *y*-axis (antiplane direction). We can clearly see the *P*- and *S*-waves reflections from the borders of the fault. The *P* wave coming back from the left- and the right-hand sides of the fault travels in the in-plane direction. The shear wave coming back from the left- and the right-hand sides of the fault is denoted by *SI* and is travelling predominantly along the in-plane direction, whereas the shear wave coming back from the top and the bottom borders is denoted by *SA* and is travelling predominantly along the antiplane direction. In addition, due to the *SI* wave propagating backward, a late reactivation of the slip after its initial arrest could also be seen on the slip velocity figures. These behaviours have also been observed by Day *et al.* (2005), and our numerical solutions seem very close to the DFM numerical solutions for all the principal processes of the rupture: nucleation; evolution; stopping phase and overshoot of stresses.

Fig. 6 displays snapshots of the slip velocity and the shear stress on the fault plane at 0.5-s time intervals. One can clearly identify in the slip velocity figures the direct waves as well as reflected ones we have previously described. Due to the choice of both initial conditions and frictional parameters, the rupture propagates at subshear regime. One can appreciate in the shear stress snapshots, the direct shear wave travelling ahead of the rupture-front peak stress.

Table 3. Frictional parameters on the fault.

Parameters	Nucleation	Outside nucleation
Initial shear stress σ_0 (MPa)	97.49	73.73
Initial normal stress $-\sigma_n$ (MPa)	120	120
Static friction coefficient $\boldsymbol{\mu_s}$	0.677	0.677
Dynamic friction coefficient $\boldsymbol{\mu_d}$	0.525	0.525
Static yielding stress $\sigma_s = -\boldsymbol{\mu_s}\,\sigma_n$ (MPa)	81.24	81.24
Dynamic yielding stress $\sigma_d = -\boldsymbol{\mu_d}\,\sigma_n$ (MPa)	63	63
Critical slip distance δ_0 (m)	0.8	0.8

5.1.1 Convergence study

To understand the influence of the mesh size on the numerical solution, we perform several comparisons between our FV solutions and a finite difference solution used in the previous section computed by Day *et al.* (2005) with a grid size of 50 m, which we consider as a reference. The comparisons are made in two points of the fault surface, belonging, respectively, to the purely in-plane and the purely antiplane axis. The in-plane receiver is located at 7.5 km from the centre of the fault plane along the strike direction, whereas the antiplane receiver is located 6 km from the centre along the dip direction.

Fig. 7 shows the shear stress and the slip velocity seismograms recorded in the in-plane and the antiplane receivers. The reference solution is plotted with a solid line, whereas various FV numerical solutions for different meshes are plotted with dashed lines. One can clearly see that the FV solution converges towards the reference solution when the mesh grid becomes smaller. Both the rupture arrival time and the arrest phase around 7 s get closer to the values of the FD solution. We also can remark that the slip velocity plots contain less oscillations when the mesh grid is refined enough.

Fig. 8 shows a comparison of the relative rms in arrival time and arrest pulse for the two receivers. Throughout the paper, we have defined the relative rms as the L^2 norm of the difference between the target and the reference solutions, divided by the L^2 norm of the reference solution. One can note that the rms difference between the FV solutions and the reference solution becomes smaller as the mesh is refined. The slopes of the regression lines are comparable, indicating a similar convergence rate for both in-plane and antiplane propagation direction. Let us note that the rms error for our finest mesh is around 0.1 for the rupture times, even if the grid size of the FV scheme is three times larger than the FD reference solution. Given the high convergence rates, we expect this error still reduced if our computing capabilities allow us to refine the mesh up to the same grid size of the reference solution (i.e. 50 m).

Finally, Fig. 9 displays the rms time difference of the shear stress and the shifted phase slip velocity compared with the reference solution at the two observation points. The slip velocity curves have been shifted to the arrival time to focus on comparisons of the global shape of the solutions (i.e. uniform convergence; for comparisons on arrival time, see Fig. 8). The slope of the regression line for the shear stress diagram, which is almost the same for both the in-plane and the antiplane receivers, is between 0.5 and 1, whereas the slope of the regression line for the slip velocity is quite different for the in-plane and the antiplane receivers. This difference could be related to the oscillating behaviour of the slip velocity solution, especially in the antiplane direction. When the mesh becomes more refined, the numerical oscillations become smaller and so is the rms difference. The seismograms in the in-plane direction exhibit less numerical oscillations and are hence less significant in the rms computation.

Although this study was carried on in two particular points on the fault surface, it reflects the general behaviour of the numerical solution over the fault plane. Convergence toward the reference solution is accomplished when the mesh grid is refined enough. In addition, the spurious oscillations due to the fault propagation are diminished. The rupture time, the arrest phase waveform and the reactivation of the slip for both in-plane and anti-plane directions are well simulated, whereas the peak of the slip velocity and the final slip are slightly underestimated. We think this is due to an insufficient space accuracy of the FV method. As clearly seen for many numerical approaches solving the same dynamic rupture problem (Harris *et al.* 2009), achieving a perfect convergence with grid size of 150 m, our finest case, is a difficult task. However, according to the high convergence rate we have determined for our scheme, we expect the FV solution for a grid size of 50 m to fit closely the reference one. An alternative issue could be the use of higher interpolation polynomials instead of a constant polynomial in each cell. We expect that the approximation of the singularity due to the rupture propagation, and hence the peak of the slip velocity, would be improved even on coarser meshes.

5.2 Test problem 2

We shall consider now the non-planar parabolic-shaped rupture problem introduced by Cruz-Atienza *et al.* (2007), for numerical comparisons. We consider a linearly elastic homogeneous medium, as for the SCEC selected case, whose characteristics were already given in Table 1. The rupture surface is a parabola in the *xz* plane, given by the equation

$$(z - z_0)^2 = (x - x_0)^2 / (4\,e)\,, \tag{81}$$

where (x_0, z_0) correspond to the vertex at the centre of the medium and $e = 10$ km is the eccentricity of the parabola. The coordinate y of the fault surface is translation invariant. A 3-D view of the fault surface is presented in Fig. 10.

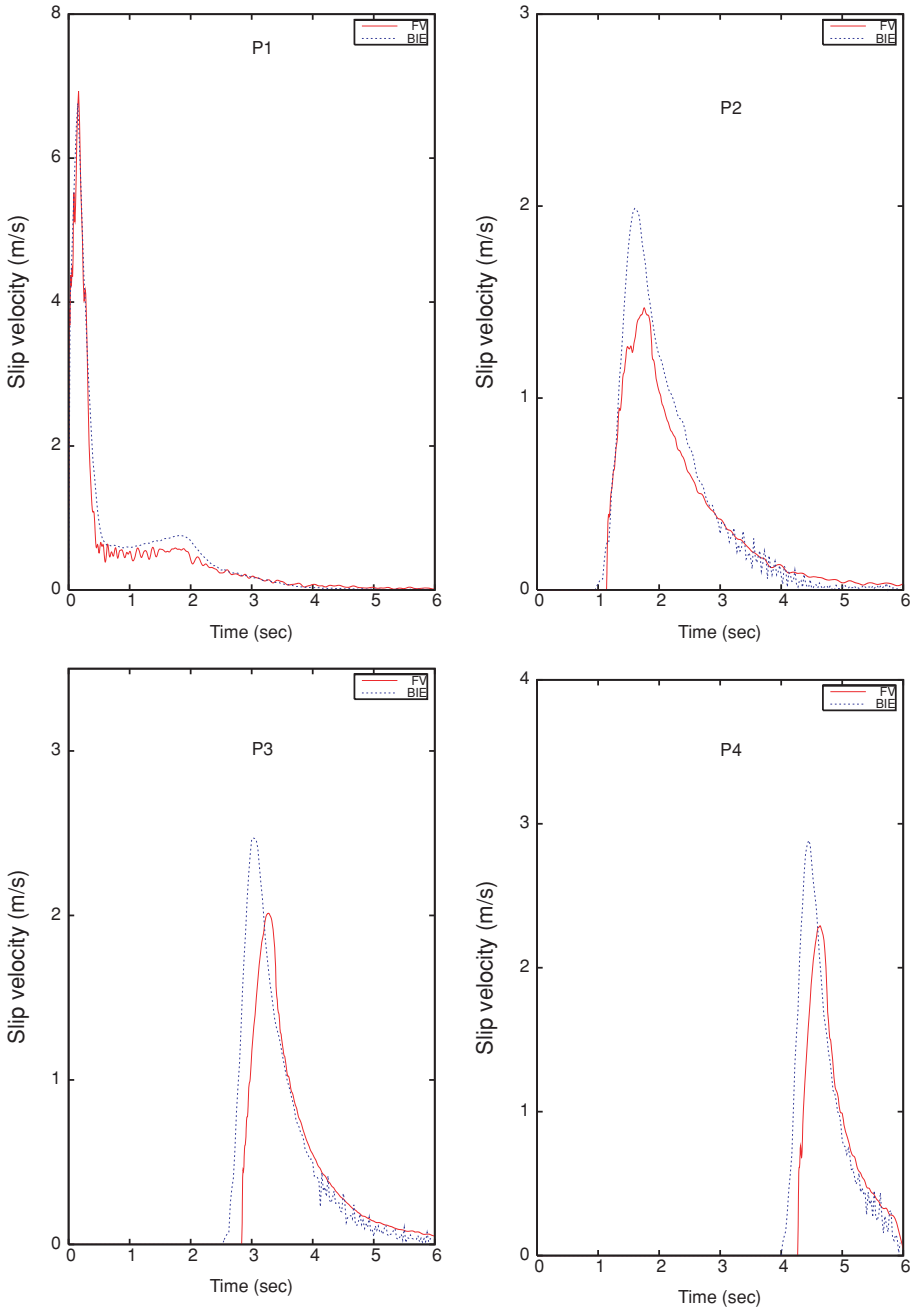

Figure 11. Comparison of the FV numerical solutions (red) and the BIE numerical solution (blue) of the slip velocity in four points located on the fault surface. Small differences are noted between the solutions. The FV solutions are filtered with diffusion coefficient $\eta = 0.2$ (see Benjemaa *et al.* 2007, for more detail).

The nucleation zone is a 'square region' of 2 km side (grey patch in Fig. 10), centred at (x_0, z_0). In this zone, the shear stress is supposed to be slightly higher than the initial static yield stress. The shear pre-stress is aligned with the dip direction and assumed to be constant along the non planar fault surface. This may suppose an extremely heterogeneous surrounding stress field. For comparisons, we choose four fault observational points placed along a line passing through the fault centre and parallel to the x-axis (in-plane direction, Fig. 10). The first point corresponds to the centre of the nucleation zone (x_0, z_0) and the other points are separated from each other by 4 km, measured over the rupture surface. We assume an infinite static frictional stress at the fault borders preventing the rupture to propagate beyond them. The constitutive parameters that govern the rupture evolution are given in Table 3.

Eq. (12) means that the friction resistance is equal to the product of the normal stress and the friction coefficient. During the rupture, and due to the fault geometry, the normal stress may change from its initial value. As a consequence, the static frictional stress μ_s may vary. Although our method is able to deal with such a feature, we chose to assume the normal stress during the rupture to be constant. Actually, this restriction is made only to mimic a former BIE simulation (Aochi *et al.* 2000) that we had taken as a reference solution. Both the static and dynamic fault strengths depend only on the initial static traction during the rupture process.

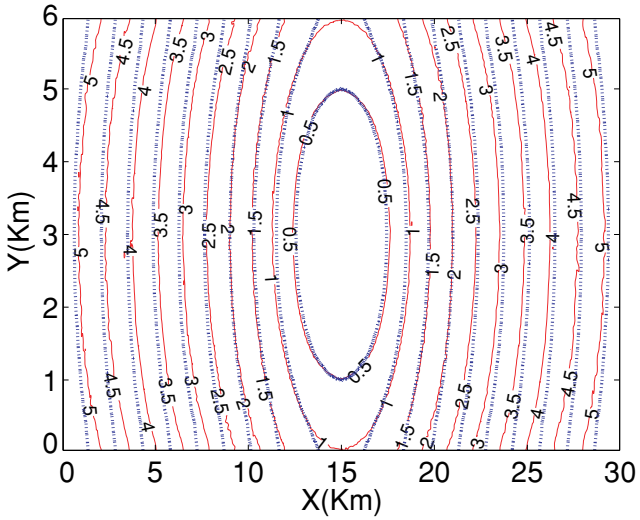

Figure 12. Rupture front contours at 0.5 s intervals computed along the parabolic fault surface for the FV (red) and the BIE (blue) methods.

To discretize the fault surface, we used an unstructured triangulation with space length approximatively equal to 0.1 km. The entire domain is then discretized by 11 million tetrahedra, including this triangulation (i.e. two tetrahedra above and below the fault share at most a unique triangle on the fault surface). Thus, no confusion of the faces belonging to the fault surface would occur. The time step is obtained with respect to a CFL criterion, and is equal to 2.1×10^{-3} (see Benjemaa *et al.* 2006, for more details about the CFL criterion) . For the BIE method, the space length is $\Delta x = 0.15$ km with a corresponding time step $\Delta t = 1.25 \times 10^{-2}$. We performed our computation over 64 processors using MPI and the CPU time of the simulation is about 2×10^3 s.

Fig. 11 shows a comparison of the slip velocity computed at four points located on the fault surface. We can see a fairly good agreement between numerical solutions. To reduce the spurious high frequency oscillations due to the rupture front propagation, we have added a diffusion term, with coefficient $\eta = 0.2$, to the elastodynamic equations. We do not discuss this additional term here, but one can find all details in Benjemaa *et al.* (2007), as it behaves similarly for 2-D and 3-D geometries. Let us remark that neither the rupture time nor the slip velocity amplitude were affected by this smoothing coefficient.

As for the first benchmark case, our method seems to slightly underevaluate the slip velocity along the fault. This is due to the unstructured mesh used for the discretization of the fault surface. In fact, Lohrengel & Remaki (2002) showed that the centred finite volume scheme (applied to Maxwell system) is second order in space, when applied to structured meshes but only of spatial half-order when applied to unstructured meshes. This fact induces some numerical dispersion in the wave propagation, which affects the accuracy of near-field seismograms and, thus, the rupture front evolution and the slip estimate. Brossier *et al.* (2008) has observed the same behaviour while studying only propagation effects of elastodynamic equations, through an identical finite volume formulation in the frequency domain, making us confident that the wave propagation is the cause of this slight misfit and not the numerical implementation of boundary conditions, as also demonstrated in the 2-D implementation (Benjemaa *et al.* 2007).

Further investigations of the influence of numerical dispersion on the rupture dynamics are necessary and should come with the investigation of higher-order interpolation techniques inside each element. The so-called discontinuous Galerkin finite elements method (DGFEM), which can be thought as a higher order version of our finite volume approach, approximates the solution of the problem in each cell as a combination of high-order polynomials inside each cell. Thus, again, no continuity is imposed from one cell to another: Fezoui *et al.* (2005) have shown for Maxwell equations, that centred DGFEM scheme is kth order in space if kth order polynomial approximation is used. First results obtained using such a scheme when studying propagation effects of the elastodynamic equations confirm this property (Delcourte *et al.* 2009). Hence, the accuracy of the solution and, particularly, the peak of the slip velocity, could be improved when using such schemes and, so, should be the rupture front evolution. Let us note that such an approach based on the arbitary high order derivatives (ADER) scheme has been developed and used by Dumbser *et al.* (2007) (see references therein) for wave propagation, with remarkable accurate results (Kaser & Dumbser 2006; Kaser *et al.* 2007). Our results, which can be seen as those obtained by the lowest-order formulation of the DGFEM approach, are already quite accurate: a new result as far as we know.

Fig. 12 shows a contour plot of the rupture time for both methods. Considering the numerical complexity involved by the spontaneous rupture of a non-planar fault and compared with a previous comparison held for the same problem by Cruz-Atienza *et al.* (2007), our rupture times are in reasonable good agreement with those computed by the BIE method. As for the first test case, more significant differences seem to appear along the antiplane direction. We expect the accuracy of the method to be improved as we move to higher-order spatial approximations of the numerical scheme.

Fig. 13 displays snapshots of the slip velocity and the shear stress on the fault plane at 0.45-s time intervals. Due to the choice of both initial stress conditions and frictional parameters, the rupture propagates at subshear regime. Looking closer at the shear stress snapshots, one can identify the direct S wave, travelling ahead of the rupture front.

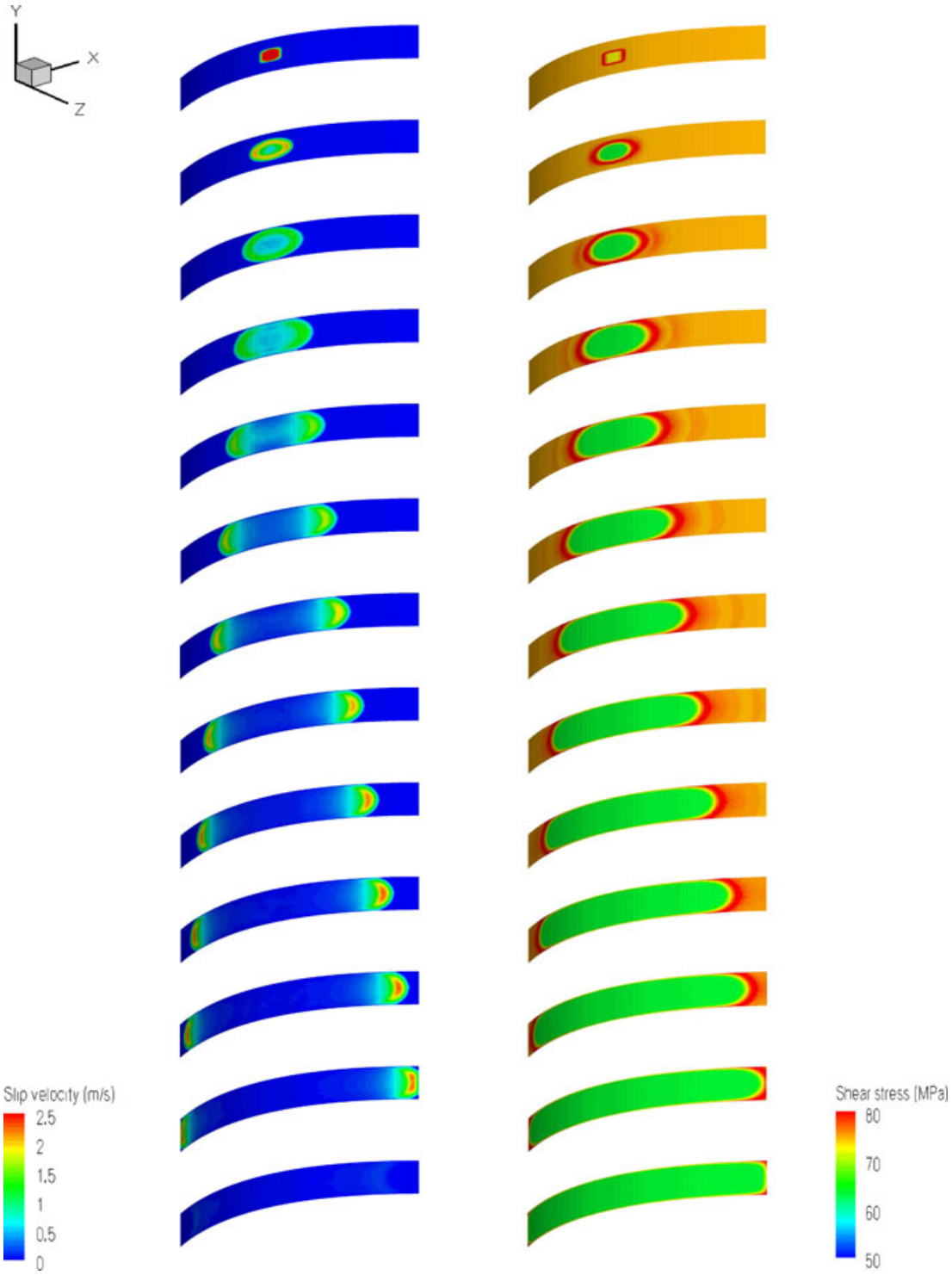

Figure 13. Snapshots of the slip velocity (left-hand panel) and the shear stress (right-hand panel) at 0.45 s time intervals along the fault.

We may conclude that, in spite of small differences, the FV method we propose has successfully solved two difficult benchmarking cases for both planar and non-planar fault geometries. This validates our approach, as well as our numerical approximation of the failure criterion on the fault surface.

6 DISCUSSION AND CONCLUSION

We have introduced a finite volume method for the simulation of the spontaneous shear rupture problem along non-planar surfaces in 3-D heterogeneous media. Thanks to an appropriate change of variables, all parameters of the medium are grouped on the left-hand side of

the elastodynamic equations, and integration can be made even when medium heterogeneities exist, as already shown in the 2-D geometry (Benjemaa *et al.* 2007). A careful analysis of a suitable discrete expression of the total energy allows us to define the appropriate fracture boundary conditions to be imposed on the crack surface. The shear traction is defined on the fault surface through fluxes in such way that no slip velocity occurs when the shear stress is less than the yield friction value. This makes the fracture to have no thickness; so, both crack blocks only interact through the fracture traction vector. Consequently, different elastic properties at both sides of the fracture can be properly considered (e.g. bi-materials cracks). Spurious high frequency content in elastic fields at the vicinity of the crack tip can be reduced when appropriate dissipation terms are added. This could be achieved without important additional memory requirement (see Benjemaa *et al.* 2007, for more details). The comparisons with results of an independent finite difference method (Day *et al.* 2005) for spontaneous planar rupture case, as well as with results of a boundary integral method (Aochi *et al.* 2000) for a non planar rupture geometry, have revealed good agreements between the solutions, validating, thus, our approach for any kind of rupture geometry. The accuracy of the solution could be improved by either refining the mesh triangulation over the fault surface or using higher order schemes based for instance on a discontinuous Galerkin method. In fact, the finite volume approach we have applied, comes from previous formulations for the electromagnetic wave propagation modelling (Remaki 2000) and can be seen as a low-order discontinuous Galerkin method based on constant basis functions (P0). We expect the solution accuracy to be improved in such formulation as we move to higher orders, but we must be aware to keep the computational efficiency we have observed in the finite volume approach, which leads us to think that the order of interpolation inside each cell should not go beyond a space scheme of second order (P1 or P2). We envision a very promising efficient technique for seismic dynamic rupture modelling in the near future.

ACKNOWLEDGMENTS

The authors are grateful to S. Lanteri for his constructive comments and his help for the parallel implementation aspects of the code.

We are thankful to the reviewers for constructive remarks and suggestions that contributed to the improvement of our original manuscript. Dr Jun Korenaga is also thanked as an associated editor.

REFERENCES

Aagaard, B., Hall, J. & Heaton, T., 2001. Characterization of near-source ground motions with earthquake simulations, *Earthq. Spectra,* **17,** 177–207.

Aki, K. & Richards, P., 1980. *Quantitative Seismology: Theory and Methods,* W.H. Freeman & Co, San Francisco.

Andrews, D., 1976. Rupture velocity of plain strain shear cracks, *J. geophys. Res.,* **81,** 5679–5687.

Andrews, D., 1985. Dynamic plane-strain shear rupture with a slip weakening friction law calculated by a boundary integral method, *Bull. seism. Soc. Am.,* **75,** 1–12.

Andrews, D., 1999. Test of two methods for faulting in finite difference calculations, *Bull. seism. Soc. Am.,* **89**(4), 931–937.

Aochi, H., Fukuyama, E. & Matsu'ura, M., 2000. Spontaneous rupture propagation of a non planar fault in 3d elastic medium, *PAGEOPH,* **157,** 2003–2027.

Bécache, E. & Duong, T.H., 1994. A space-time variational formulation for the boundary integral equation in a 2D elastic crack problem, *J. geophys. Res.,* **28,** 141–176.

Benjemaa, M., Piperno, S. & Glinsky-Olivier, N., 2006. Étude de stabilité d'un schéma volumes finis pour les équations de l'élastodynamique en maillages non structurés, RR-5817, INRIA Sophia Antiplois, France.

Benjemaa, M., Glinsky-Olivier, N., Cruz-Atienza, V.M., Virieux, J. & Piperno, S., 2007. Dynamic non-planar crack rupture by a finite volume method, *Geophys. J. Int.,* **171**(1), 271–285.

Brossier, R., Virieux, J. & Operto, S., 2008. Parsimonious finite-volume frequency-domain method for 2-D *P-SV*-wave modeling, *Geophys. J. Int.,* **175**(2), 541–559.

Cruz-Atienza, V.M. & Virieux, J., 2004. Dynamic rupture simulation of non-planar faults with a finite-difference approach, *Geophys. J. Int.,* **158,** 939–954.

Cruz-Atienza, V.M., Virieux, J. & Aochi, H., 2007. 3D finite-difference dynamic-rupture modelling along non-planar faults, *Geophysics,* **72**(5), 123–137.

Dalguer, L. & Day, S.M., 2007. Staggered-grid split-node method for spontaneous rupture simulation, *J. geophys. Res.,* **112**(B2), doi:10.1029/2006JB004467.

Das, S. & Aki, K., 1977. A numerical study of two-dimensional spontaneous rupture propagation, *Geophys. J. R. astr. Soc.,* **50,** 643–668.

Day, S., 1977. Finite element analysis of seismic scattering problems, *PhD Dissertation,* California University, San Diego.

Day, S., 1982. Three-dimensional simulation of spontaneous rupture: the effect of nonuniform prestress, *Bull. seism. Soc. Am.,* **72,** 1881–1902.

Day, S., Dalguer, L.A., Lapusta, N. & Liu, Y., 2005. Comparison of finite difference and boundary integral solutions to three-dimensional spontaneous rupture, *J. geophys. Res.,* **110**, B12307.

Delcourte, S., Fezoui, L. & Glinsky-Olivier, N., 2009. A high-order discontinuous galerkin method for the seismic wave propagation, ESAIM: Proceedings, accepted.

Dumbser, M., Käser, M. & Toro, E., 2007. An arbitrary high order discontinuous galerkin method for elastic waves on unstructured meshes, V: local time stepping and *P-additivity, Geophys. J. Int.,* **171**(2), 695–717.

Festa, A. & Vilotte, J.-P., 2006. Influence of the rupture initiation on the intersonic propagation: crack-like versus self-healing pulses, *Geophys. Res. Lett.,* **33,** L15320, doi:10.1029/2006GL026378.

Fezoui, L., Lantéri, S., Lohrengel, S. & Piperno, S., 2005. Convergence and stability of a discontinuous galerkin time-domain method for the 3D heterogeneous maxwell equations on unstructured meshes, *ESAIM,* **39,** doi:10.1051/m2an:2005049.

Harris, R.A. *et al.*, 2009. The SCEC/USGS dynamic earthquake-rupture code verification exercise, *Seismol. Res. Lett.,* **80**(1), 119–126.

Huang, H. & Costanzo, F., 2004. On the use of space-time finite elements in the solution of elasto-dynamic fracture problems, *Int. J. fract.,* **127,** 119–146.

Ida, Y., 1972. Cohesive force across the tip of a longitudinal-shear crack and griffith's specific surface energy, *J. geophys. Res.,* **77,** 3796–3805.

Kaser, M. & Dumbser, M., 2006. An arbitrary high order discontinuous galerkin method for elastic waves on unstructured meshes, I: the two-dimensional isotropic case with external source terms, *Geophys. J. Int.,* **166**(2), 855–877.

Kaser, M., Dumbser, M., de la Puente, J. & Igel, H., 2007. An arbitrary high order discontinuous galerkin method for elastic waves on unstructured meshes, III: viscoelastic attenuation, *Geophys. J. Int.,* **168**(1), 224–242.

Komatitsch, D. & Vilotte, J.-P., 1998. The spectral element method: an efficient tool to simulate the seismic response of 2-D and 3-D geological stuctures, *Bull. seism. Soc. Am.,* **88,** 368–392.

Lohrengel, S. & Remaki, M., 2002. A finite volume scheme for Maxwell's equations. Convergence analysis on unstructured meshes, in *Finite Volume for Complex Applications,* Vol. III, eds Herbin, R. & Kroner, D., Kogan. Hermes Penton Science, London, Porquerolles, 219–226.

Madariaga, R., 1976. Dynamics of an expanding circular fault, *Bull. seism. Soc. Am.,* **66,** 639–666.

Oglesby, D.D. & Archuleta, R.J., 2003. The three-dimensional dynamics of a nonplanar thrust fault, *Bull. seism. Soc. Am.,* **93,** 2222–2235.

Palmer, A. & Rice, J., 1973. The growth of slip surfaces in the progressive failure of overconsolidated clay slopes, *Proc. R. Soc. Lond.,* **A332,**, 527–548.

Remaki, M., 2000. A new finite volume scheme for solving maxwell system, *COMPEL,* **19**(3), 913–932.

Tada, T. & Madariaga, R., 2001. Dynamic modelling of the flat 2-D crack by a semi-analytical BIEM scheme, *Int. J. Numer. Methods Eng.,* **50,** 227–251.

Tada, T. & Yamashita, T., 1997. Non-hypersingular boundary integral equations for two-dimensional non-planar crack analysis, *Geophys. J. Int.,* **130,** 269–282.

Virieux, J., 1986. *P-SV* wave propagation in heterogeneous media, velocity-stress method, *Geophysics,* **51,** 889–901.

Virieux, J. & Madariaga, R., 1982. Dynamic faulting studied by a finite difference method, *Bull. seism. Soc. Am.,* **72,** 345–369.